Highly dispersed PdS preferably anchored on In_2S_3 of MnS/In_2S_3 composite for effective and stable hydrogen production from H_2S

Yi Li[a,b], Shan Yu[a,b,*], Dmitry E. Doronkin[c], Shiqian Wei[a,b], Meng Dan[a,b], Fan Wu[a,b], Liqun Ye[d], Jan-Dierk Grunwaldt[c], Ying Zhou[a,b,*]

[a]State Key Laboratory of Oil and Gas Reservoir Geology and Exploitation,

Southwest Petroleum University,

Chengdu 610500, China.

Email: yzhou@swpu.edu.cn (Ying Zhou)

Email: yushan@mail.ipc.ac.cn (Shan Yu)

[b]The Center of New Energy Materials and Technology,

School of Materials Science and Engineering,

Southwest Petroleum University,

Chengdu 610500, China.

[c]Institute for Chemical Technology and Polymer Chemistry and Institute of Catalysis Research and Technology,

Karlsruhe Institute of Technology,

76131 Karlsruhe, Germany.

[d]Engineering Technology Research Center of Henan Province for Solar Catalysis,

Collaborative Innovation Center of Water Security for Water Source Region of Mid-line of South-to-North Diversion Project of Henan Province,

Nanyang Normal University,

Nanyang 473061, China.

Abstract

As an important byproduct during natural gas exploitation, green utilization of hydrogen sulfide (H_2S) by photocatalysis has offered us the possibility for production of clean hydrogen (H_2) from H_2S with low energy consumption. In this work, we have successfully introduced well-dispersed palladium sulfide (PdS) which is preferably loaded on In_2S_3 of MnS/In_2S_3 composite for improved photocatalytic hydrogen evolution from H_2S aqueous solution. In contrast to binary MnS/In_2S_3, ternary $MnS/In_2S_3/PdS$ has exhibited a remarkable and stable hydrogen production rate of 22.7 mmol g^{-1} h^{-1} with an apparent quantum yield of 34 % at around 395 nm. A comprehensive structure characterization of the ternary composite including scanning transmission electron microscopy (STEM) and X-ray absorption spectroscopy (XAS) in combination with theoretical calculations confirm the good dispersion of PdS in the composite. Moreover, we discovered that PdS preferably interact with In_2S_3 rather than MnS in the composite through Pd-S-In bond on the interface of the two. Photoluminescence (PL) spectra, surface photovoltage (SPV) spectra together with transient photocurrent and electrochemical impedance spectra (EIS) demonstrate the advantage of PdS for promoting the charge separation. This work sheds light on the positive effect on the enhanced activity of the corresponding system resulting from the preferable anchoring of highly dispersed PdS on In_2S_3 in the composite by chemical Pd-S-In bond. Not only the high dispersion but also the preferable anchoring of the co-catalyst in the composite could hence inspire people for more rational designs of ternary composite in future.

Keywords：photocatalysis; hydrogen production; metal sulfide; preferable deposition; high dispersity;

1. Introduction

Hydrogen sulfide (H_2S), largely produced in oil and gas exploitation, has attracted great attention focused on its efficient removal because of its corrosive properties and high toxicity (LC_{50} approximately 500 ppm) [1-3]. H_2S is largely produced in the hydrodesulfurization process of heavy oil during exploitation, in which hydrogen (H_2) is consumed [4]. On the other hand, from the standpoint of sustainable energy production, H_2S is regarded as a good resource resulting from its special elemental composition. In terms of H_2S conversion, various techniques have been proposed. Traditionally, H_2S is handled in industry with the Claus process [5], in which H_2S is converted to sulfur and H_2O. But one should be aware of the potential of hydrogen contained in H_2S as well. Accordingly, other methods that focus on collection of H_2 from H_2S have been developed [6-11]. Among them, photocatalysis is regarded as a promising technique due to its potential for direct conversion of solar energy into clean fuels [12-20]. Using photocatalysis one can recover the consumed H_2 and recycle it back in the hydrodesulfurization. Notably, photocatalytic hydrogen evolution from H_2S is thermodynamically more favorable compared to traditional photocatalytic H_2O splitting: ΔG for H_2S splitting (39.4 kJ mol^{-1}) is far less than that for water splitting (284.7 kJ mol^{-1}) [21]. Hence, there is a broader choice for the photocatalysts which could promote H_2S decomposition.

Among various kinds of photocatalysts, metal sulfides exhibit many advantages due to their suitable band structure and strong visible-light absorption. Many research works focused on sulfides such as CdS [22-25], ZnS [26], $CuInS_2$ [27] have been reported; meanwhile, the development of other metal sulfides is necessary [28]. In our previous work [29], we discovered that MnS/In_2S_3 composite is an effective photocatalyst for hydrogen evolution from H_2S in the visible light region. Nevertheless, the catalytic activity of MnS/In_2S_3 is insufficient for practical application and further optimization is required. Introduction of noble metal co-catalyst such as Pt [30] and Pd [31, 32] for promotion of charge separation efficiency as well as surface reaction kinetics is

a widely recognized method for improving the photocatalytic efficiency. However, the poisoning effect of H_2S, which can inhibit the activity of noble metals [33-35], makes it difficult to directly utilize Pt or Pd in H_2S related research. Hence, noble metal sulfides [36] were used instead due to their more resistant properties to the harsh sulfidizing environment compared to pure noble metals.

In order to boost the photocatalytic efficiency of MnS/In_2S_3 for decomposition of H_2S, palladium sulfide (PdS) could be selected as the cocatalyst for improved charge separation accordingly. In previous report, the role of PdS in photocatalysis has been revealed to facilitate transfer of photogenerated holes on metal sulfides [37], and PdS has been reported to be a good co-catalyst when combined with CdS [38], $Zn_{0.5}Cd_{0.5}S$ [39] and $ZnS-CuInS_2$ [40]. However, traditional co-catalysts are prone to agglomeration during the activation and photocatalysis [41, 42] decreasing the atomic efficiency of earth-scarce palladium. To better exploit palladium, the size of co-catalyst particles should be decreased to clusters or even to single atoms [43, 44], so that the fraction of accessible active sites during photocatalysis could be maximized. More importantly, when the size of the co-catalyst particles is small enough, additional interaction between the co-catalyst and the substrate has been reported in a series of works [45]. For example, it was also found that single Pd atom strongly interacts with TiO_2 and such interaction plays a crucial role in preventing the sintering of Pd atoms [46]. Hence, it is of great importance to prepare ultrasmall and well-dispersed PdS co-catalyst on MnS/In_2S_3 for photosplitting of H_2S.

In this work, we report on highly dispersed PdS anchored as a co-catalyst on In_2S_3 of the MnS/In_2S_3 composite. Introduction of PdS improved the efficiency of photocatalytic hydrogen evolution from H_2S aqueous solution by approximately 6 times, reaching hydrogen evolution rate of 22.7 mmol g^{-1} h^{-1} and an apparent quantum yield (AQY) of 34% at around 395 nm. Comprehensive in-depth characterization including scanning transmission electron microscopy (STEM), X-ray photoelectron

spectroscopy (XPS) and X-ray absorption spectroscopy (XAS) were presented for uncovering the structure of Pd species and their interaction with MnS/In$_2$S$_3$. Pd-In-S interaction was detected in the system and theoretical calculations were furthermore employed to analyze the formation mechanism of the bonds. Finally, photoluminescence (PL) spectroscopy, surface photovoltage (SPV) spectroscopy, photoelectrochemical tests in addition to density functional theory (DFT) calculations revealed that PdS sites in the composite also facilitate the photogenerated charge separation and the removal of oxidation product, which indicates the potential of noble metal sulfides in sustainable utilization of H$_2$S.

2. Experiments

2.1 Materials:

Manganese acetate (Mn(CH$_3$COO)$_2$·4H$_2$O), indium chloride (InCl$_3$·4H$_2$O), palladium chlorid (PdCl$_2$) are purchased from Aladdin (Shanghai, China). Thioacetamide (TAA) was supplied by Alfa Aesar. Sodium sulphide (Na$_2$S·9H$_2$O), hydrochloric acid (HCl) and pyridine (C$_5$H$_5$N) were purchased from Chron Chemicals (Chengdu, China). All of the materials were used as received without further purification.

2.2 Synthesis of MnS/In$_2$S$_3$ composite:

MnS/In$_2$S$_3$ was prepared using the method reported previously [29]. Typically, 1.4 mmol manganese acetate, 0.6 mmol indium chloride and 9.0 mmol thioacetamide were dissolved in 25 mL pyridine to obtain a homogeneous solution with continuous stirring. Then the transparent solution was transferred into a 25 mL Teflon-lined stainless steel autoclave, which was maintained at 180 °C for 30 h. The product was then collected and washed with ethanol under ultrasound. After centrifugation and drying under vacuum at 60 °C overnight, a dark yellow powder was obtained. α-MnS and β-In$_2$S$_3$ were synthesized using the same technique with only manganese acetate or indium chloride added, respectively.

2.3 Preparation of PdS/MnS/In$_2$S$_3$ composite:

200 mg MnS/In$_2$S$_3$ composite powder was dispersed in 50 mL deionized water with ultrasonic treatment for 0.5 h. Then 3 mL isopropanol and 0.375 mL palladium chloride solution (with a concentration of 8 mg Pd/mL, prepared in 0.57 M HCl solution) were added dropwise to the suspension. After that, the suspension was transferred to a 50 mL glass flask. With continuous stirring and Ar gas flow, the flask was irradiated by a 300 W Xe lamp for 2 h. Ultimately, the 1.5 wt.% Pd-MnS/In$_2$S$_3$ composite was collected, washed with ethanol for several times and dried at 60 ^{o}C overnight. Here 1.5 wt.% means the weight ratio of introduced Pd to MnS/In$_2$S$_3$ composite. In this way, MnS/In$_2$S$_3$ composites loaded with various amounts of Pd precursor were obtained. For convenience, MI-Pd X% (X = 0.2 ~ 2) were used to represent the MnS/In$_2$S$_3$ composites with different amount of noble metal precursors added during the preparation. As a reference, MI stands for MnS/In$_2$S$_3$ composite treated in the same way but without addition of the Pd precursor. Fig. S1 shows the photos of MI and MI-Pd 1.5%, noting that the color of sample turned dark yellow from light yellow after introduction of Pd species. Additionally, α-MnS and β-In$_2$S$_3$ loaded with 1.5 wt.%% Pd were obtained by the same procedure.

2.4 Photocatalytic tests:

The photocatalytic performance tests were conducted using a home-built setup [29]. At first, the system was flushed with Ar. Then 150.0 mL of HCl solution (2.0 mol/L) was added dropwise into 150.0 mL Na$_2$S solution (1.0mol/L) to produce H$_2$S gas in 3 - 4 h. The H$_2$S gas was directly bubbled into a 50 mL flask which contains 50 mL Na$_2$S (0.1 mol/L) and Na$_2$SO$_3$ (0.6 mol/L) solution as well as 2.5 mg photocatalyst. Subsequently, the flask was sealed and then irradiated by a 300 W Xe lamp with a cutoff filter (λ > 420 nm). The hydrogen production rate was monitored using a Shimadzu GC-2010 Plus gas chromatograph (GC) (Ar carrier gas, molecular sieve 5 Å columns, TCD detector).

The apparent quantum yield (AQY) of sample was calculated using Eq. 1. The number of incident photon was defined by using monochromatic LED lamps (cf. Table S1).

$$AQY\ (\%) = \frac{number\ of\ reacted\ electrons}{number\ of\ incident\ photons} \times 100\%$$

$$= \frac{number\ of\ hydrogen\ molecules\ \times 2}{number\ of\ incident\ photons} \times 100\%$$

Eq.1

2.5 Photoelectrochemical tests:

Photoelectrochemical tests were carried out on a CHI660E electrochemical workstation (Chenhua Instrument, Shanghai, China) equipped with a standard three-electrode system. The working electrode was prepared by doctor-blade coating method on fluorine doped tin oxide (FTO) with a film thickness of about 50 μm and area of 4 cm^2, which was further treated at 200 ºC for 3 h in Ar. Pt wire was used as the counter electrode and a saturated calomel electrode (SCE) was the reference electrode. Na_2SO_3 solution in water (1.2 mol/L) was used as the electrolyte.

2.6 Characterization:

The crystal structure and crystallinity of the samples were studied by X-ray diffraction (XRD) with Cu Kα radiation using Philips X'Pert diffractometer operated at 40 kV and 40 mA. The optical properties were investigated by ultra-violet and visible light (UV-vis) diffuse reflectance spectroscopy (DRS) and photoluminescence (PL) spectroscopy. UV-vis DRS was carried out on a Shimadzu UV-2600 spectrophotometer equipped with an integrating sphere and $BaSO_4$ was used as a reflectance standard. PL spectra were obtained on a Hitachi F-7000 fluorescence spectrophotometer. Transmission electron microscopy (TEM, Tecnai G2 F30) was used to investigate the morphology and nanostructure. High-angle annular dark field (HAADF) images and energy dispersive X-ray spectra (EDS) were recorded on a JEOL ARM200CF with a dual-type EDS detector (JED-2300T) and a FEI

Titan spherical aberration corrected scanning transmission electron microscope (STEM). X-ray photoelectron spectroscopy (XPS) measurements were performed using a Thermo ESCALAB 250Xi X-ray photoelectron spectrometer using Al Kα radiation and all binding energies were referenced to the C 1s peak at 284.8 eV. The pass energy for survey spectra and fine spectra are 150 eV and 30 eV, respectively. The N_2 adsorption isotherms and Brunauer-Emmett-Teller (BET) surface areas were determined by the nitrogen adsorption method with Quadrasorb SI. The samples were degassed at 110 °C for 8 h under vacuum before measurements. Surface photovoltage (SPV) measurements were recorded using an Omni - λ 3007 monochromatic-light, including a lock-in amplifier (SR830, Stanford research systems, Inc.), a light chopper and a chamber.

X-ray absorption spectra (XAS) in terms of X-ray absorption near edge structure (XANES) and extended X-ray absorption fine structure (EXAFS) were measured at the CAT end station of the CAT-ACT beamline at the Synchrotron Radiation Source at KIT, Karlsruhe [47]. The samples were measured ex situ at the Pd K absorption edge in transmission mode in form of pellets (53 mg of sample, diameter 5 mm). The beam size was 0.9 mm (vertical) × 1 mm (horizontal). The spectra were normalized and the EXAFS background subtracted and Fourier-transformed (in the k-range $3 – 13.5$ Å^{-1}) using the ATHENA program from the IFFEFIT software package [48]. XANES spectra were modeled using multiple scattering FEFF 9.6.4. ab initio code [49]. For the PdS spectrum three calculations were performed by using PdS model structure (ICSD collection code 61063) and calculating spectra for all three inequivalent Pd sites. The spectra were then averaged taking into account the corresponding multiplicities. For Pd-doped In_2S_3 model, the calculations were conducted only for a tetrahedral site (according to the EXAFS suggesting 4 neighbouring S atoms) in a β-In_2S_3 framework (ICSD collection code 202353). For Pd-doped MnS sphalerite, literature-reported model structure (ICSD collection code 76205) doped with nuclear Pd was chosen based on the first shell coordination

number 4 and the matching XRD pattern. For the PdS anchored on the surface of In_2S_3 and MnS model structures optimized by DFT calculations were used. Radii of the clusters for self-consistent potential calculations (SCF) and for full multiple scattering calculations (FMS) were set as 5 Å. The position of the white line maximum in the theoretical spectra was aligned to the experimental spectra. First shell EXAFS analysis was performed using ARTEMIS (IFFEFIT) [48] and a least square method in R-space (using k, k^2, k^3-weighted data) between 1.0 and 2.5 Å. DFT optimized Pd-doped In_2S_3 and PdS anchored on In_2S_3 were used as model structures and the coordination numbers, interatomic distances, energy shift (δE_0) and mean square deviation of interatomic distances (σ^2) were refined. The absolute misfit between theory and experiment was expressed as ρ.

2.7 DFT computational method:

The density functional theory (DFT) calculations were performed using the Materials Studio software, and Cambridge Sequential Total Energy Package (CASTEP) [50] was used for the geometry optimization by the generalized gradient approximation (GGA) with Perdew-Burke-Ernzerhof (PBE) functional [51, 52]. The electron wave functions were expanded using plane waves with a cutoff energy of 300 eV, and the convergence criteria for the residual force and energy on each atom during structure relaxation were set to be 0.05 eV/Å and 2.0×10^{-5} eV, respectively. A vacuum space of 15 Å was set to separate the interaction with the periodic images. The models which were used for calculation were α-MnS (100) (JCPDS 40-1289) and β-In_2S_3 (0012) (JCPDS 25-0390). The formation energy (E_{FA}) of different configurations was calculated as follows:

$$E_{FA} = E_f - E_a - E_b \qquad\qquad \text{Eq. 2}$$

where E_f was the total energy of final configuration, and E_a and E_b were the energies of separated structures, respectively. The adsorption energies (E_{AS}) of sulfur on Pd and PdS were calculated as follows:

$$E_{AS} = E_m - E_{slab} - E_s \qquad\qquad \text{Eq. 3}$$

where E_m was the total energy of ultimate adsorption configuration, and E_{slab} was the total energy of the clean slab and E_s was the energy of S atom.

3. Results and discussion

3.1 Photocatalytic H_2 evolution efficiency from H_2S saturated solution

Pd species were introduced on MnS/In_2S_3 (abbreviated as MI) composite by photodeposition method. Photocatalytic hydrogen evolution from saturated H_2S aqueous solution was then carried out with the as-obtained MI-Pd composite. Fig. 1(a) shows that introduction of Pd species could effectively promote the hydrogen evolution rate of MI, which reaches 22.7 mmol g^{-1} h^{-1} within 5 h at 1.5 wt.% Pd (denoted as MI-Pd 1.5%) under Xe lamp irradiation ($\lambda > 420$ nm). Further increase of Pd precursor species to 2 wt.% in the system did not improve the hydrogen evolution efficiency any more, probably due to a possible shielding effect and loss of active sites. Isotopic experiments with deuterium water (D_2O) and H_2S gas shows that H_2, HD, and D_2 coexist in the evolved gas, which is in agreement to previous report (see Fig. S2 and S3 in supplementary data for more details) [53]. AQY of the system was thus measured based on the MI-Pd 1.5% using a series of monochromatic LED light sources (see more information in Table S1). Fig. 1(b) proves that the trends of AQY values under different wavelength matches well with the light absorbance of MI-Pd 1.5%, and this demonstrates that such hydrogen evolution indeed results from the photoexcitation of the composite. A highest AQY value of 34% was obtained at around 395 nm, where the absorbance of MI-Pd 1.5% is also close to the maximum. Moreover, the stability of the system is an important factor for evaluation of the system. As shown in Fig. 1(c), the photocatalytic activity of MI-Pd 1.5% is well maintained during 10 h. Cyclic tests of MI-Pd 1.5% were carried out as well (Fig. 1d), which further confirm the stability and obviously improved activity of as-prepared samples in the H_2S-rich system (a comparison of activity reported in this work and in other publications as well as

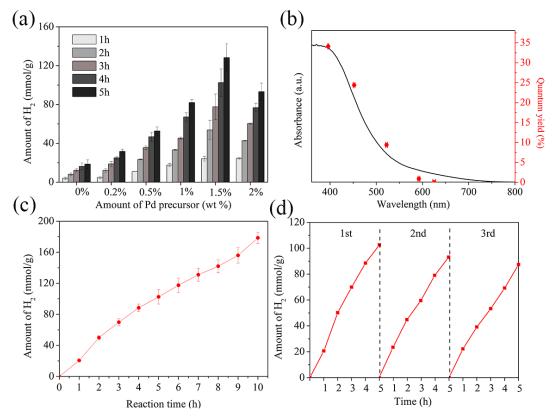the AQY and hydrogen evolution rate of reference sample CdS-Pt are given in Table S2 and S3).

Fig. 1 Photocatalytic hydrogen production rate of MI, and MI-Pd X % (X = 0.2 ~ 2) (a); ultra-violet and visible light diffuse reflectance spectra and apparent quantum yield at different wavelength of MI-Pd 1.5 % (b); 10 h long period photocatalytic hydrogen production rate of MI-Pd 1.5 % (c); three rounds cyclic photocatalytic hydrogen production rate of MI-Pd 1.5 % (d)

3.2 Structural characterization of MI-Pd

To shed light on the origins of the activity of MI-Pd, structure and optical properties of the composites were studied. XRD patterns of all MI-Pd samples were similar, with the main reflections indexed to γ-MnS and β-In$_2$S$_3$ (Fig. 2a). No obvious reflections related to any Pd species were observed even if the amount of Pd precursor reaches 2%. This may be attributed to the small size and high dispersion of Pd species. In spite of this, UV-vis DRS indicates that the light absorption in the 450 - 700 nm region slightly increases with the increased amount of introduced Pd species indicating the successful

incorporation of Pd species into MI composite. Nevertheless, the exact structure of the Pd species in the system could be barely recognized with the UV-vis DRS data.
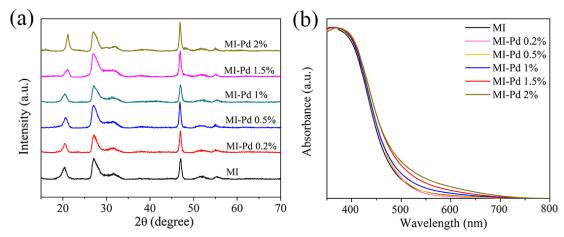

Fig. 2 X-ray diffraction pattern (a) and ultra-violet and visible light diffuse reflectance spectra (b) of MI, and MI-Pd X% (X = 0.2 ~ 2)

Morphology was then studied through TEM and spherical aberration corrected STEM to further explore the micro-structure and the possible Pd species in the composite. In particular, the composite with the highest photocatalytic activity, MI-Pd 1.5%, was deeper investigated. Typically, MI-Pd 1.5 % has a lamellar structure (Fig. 3a) [29], which resembles the original MnS/In$_2$S$_3$ composite. It is worth noting that no extra particles or clusters can be observed on the surface of MI-Pd 1.5 %. Additionally, only two diffraction rings assigned to the (002) facet of γ-MnS and (2212) facet of β-In$_2$S$_3$ were observed in the selected area electron diffraction (SAED) patterns (Fig. 3b), which agrees with the XRD results. In Fig. 3(c), highly resolved lattice fringes were clearly observed for MI-Pd 1.5% in HAADF mode, which were related to the (224) and (1019) facets of β-In$_2$S$_3$. EDS elemental mapping was then used to obtain element distribution in MI-Pd 1.5%. Pd was successfully detected homogeneously distributed in the whole studied area (Fig. 3d and e). Meanwhile, Mn, In and S elements were also clearly visible with uniform distribution as a result of the intimate junction of MnS and In$_2$S$_3$. O was also observed in the measurement, which probably originated from the absorbed

water molecules and hydroxyl groups on the surface of the composite. Based on the above data, it is reasonable to judge that ultrasmall and highly dispersed Pd species exist in MI-Pd 1.5%.
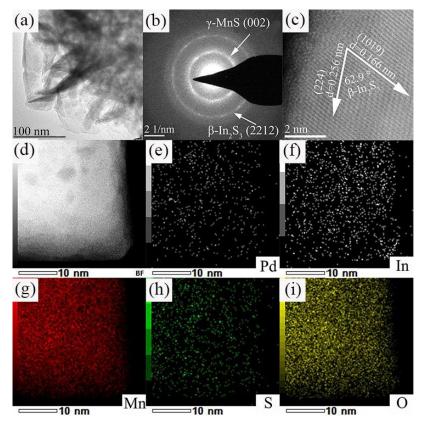

Fig. 3 Transmission electron microscope image (a), selected area electron diffraction (beam diameter: 200 nm) image (b), spherical aberration corrected scanning transmission electron microscope atomic resolution high-angle annular dark-field image (c), and energy dispersive X-ray spectrum element maps - selected area (d), element Pd (e), element In (f), element Mn (g), element S (h), element O (i) of MI-Pd 1.5%

Furthermore, the chemical state of the elements in the composite surface was revealed by XPS. Fig. 4 displays the XPS spectra of different elements of MI and MI-Pd 1.5% (see survey spectra in Fig. S4). Distinct signal of Pd could be observed in the MI-Pd 1.5% (Fig. 4a). In particular, the fine spectra of Pd exhibit one doublet peak at 337.3 eV and 342.5 eV [54] which corresponds to the 3d 5/2 and 3d 3/2 lines of Pd^{2+}, respectively. No signal belonging to Pd^0 could be obtained, illustrating absence of elemental Pd. Besides, for the fine spectra of O 1s (Fig. S5a), the peak of lattice oxygen at around 530.3 eV, characteristic of oxide [55], was not detected as well. Hence, the possible

existence of PdO in MI-Pd 1.5% was excluded either. Interestingly, we find that, compared to the original MI, the In 3d lines in MI-Pd 1.5% shifted to a higher binding energies, from 444.9 (3d 5/2) and 452.5 (3d 3/2) eV [56] to 445.1 and 452.7 eV, respectively (Fig. 4b), while those of Mn 2p remain unchanged (Fig. S5b). Such trends are further confirmed by the Mn 2p and In 3d fine spectra of other MI-Pd composites (Fig. S5b and S6b). Judging from the electronic state changes of In in MI-Pd 1.5%, the introduced Pd species may have a strong interaction with In_2S_3 in the composite. In contrast, the interaction between Pd species and MnS is weak. Binding energy of S 2p also shifted to a higher value from 161.5 (2p 3/2) and 162.7 (2p 1/2) eV to 161.9 and 163.0 eV after addition of Pd species (Fig. 4c and S6c). Accordingly, we propose that Pd is probably anchored as PdS in the MI-Pd 1.5% composite.
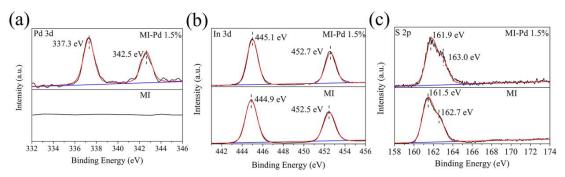

Fig. 4 X-ray photoelectron fine spectra Pd 3d (a), In 3d (b), and S 2p (c) of MI, and MI-Pd 1.5%

XAS of MI-Pd 1.5% at the Pd K edge were recorded to further verify the existence of PdS. Fig. 5(a) demonstrates that XANES spectrum of Pd in MI-Pd 1.5% differs from that of the reference Pd^0 significantly, but strongly resembles that of the reference PdS sample (crystalline PdS from Alfa Aesar, 99% purity). Based on this, existence of Pd^0 in MI-Pd 1.5% was further excluded and the chemical nature of Pd species in MI-Pd 1.5% should be very similar to PdS. Here, small differences between the spectra of MI-Pd 1.5% and PdS in the range of 24370-24380 eV may result from the high dispersion of PdS and its possible interaction with MnS/In_2S_3 composite. EXAFS spectra of MI-Pd 1.5% are also very similar to the PdS spectrum, in a good agreement with that of the

XANES data (Fig. 5b). The amplitude of oscillations is almost same, and this means that number of S atoms around Pd in the composite is the same as in PdS (4 nearest neighbors). Furthermore, Fourier-transformed (FT) EXAFS (Fig. 5c) reveals that the first coordination shell of Pd (S neighbors, approx. 1.9 Å uncorrected distance) in MI-Pd 1.5% is identical to that of PdS, which again demonstrates that the number of S atoms around Pd and the distance between Pd and S in MI-Pd 1.5% are identical to PdS (Table S4). However, an in-depth examination of the further shells (most notably, the region between 3 - 4 Å, uncorrected for the phase shift) reveals differences between MI-Pd 1.5% and the reference PdS. Therefore, PdS species in MI-Pd possibly have chemical interactions with In_2S_3 or MnS in the composite.

Due to very complex geometry of the In_2S_3 and MnS models (several overlapping shells at 3 - 4 Å) and the limited number of independent data points in the given range, full EXAFS analysis is unlikely to clearly distinguish the possible interaction between PdS and In_2S_3 or MnS. Hence, XANES modeling was employed to identify the structure and location of PdS species in the composites. Here, we used bulk Pd-doped In_2S_3 (only tetrahedral site in β-In_2S_3 was taken into account), Pd-doped MnS, as well as DFT optimized isolated PdS anchored on the surface of In_2S_3 and MnS (in all of which Pd-S bond existed) for the modeling, and the calculated XANES spectra are compared against the experimental ones (Fig. 5a and d, Fig. S7). Typically, XANES modeling does not reproduce absolute energies reliably; however, relative positions of the spectral features are well reproduced. The results show that the relative peak positions and the shape of the experimental spectrum of MI-Pd 1.5% are closer to the theoretical spectra of the Pd-doped In_2S_3 model or PdS anchored on In_2S_3 surface, rather than that of Pd-doped MnS. Consequently, PdS species in MI-Pd 1.5% should mainly interact with In_2S_3 instead of MnS. This conclusion is supported by the XPS data.
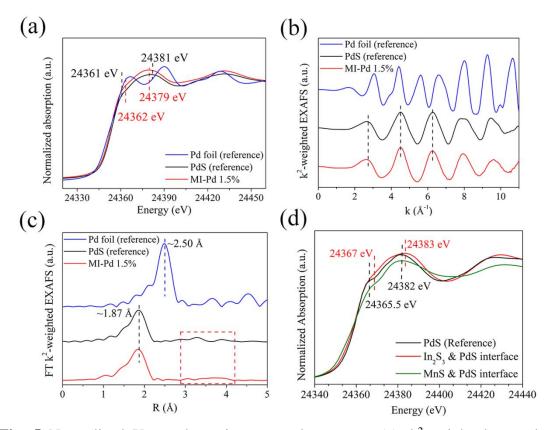
Fig. 5 Normalized X-ray absorption near edge spectra (a), k^2-weighted extended X-ray absorption fine spectra (b), and Fourier-transformed k^2-weighted extended X-ray absorption fine spectra (c) of MI-Pd 1.5% (fresh), Pd foil reference and PdS reference; theoretical X-ray absorption near edge spectra (d) of In_2S_3 & PdS interface, MnS & PdS interface and PdS reference

XPS and EXAFS data bring forward that the model of PdS anchored on In_2S_3 surface results in a good fit to the experimental spectrum (Fig. S8 and Table S4). Such a result was further supported by DFT calculations (Fig. S9 and Table S5). The formation energy of Pd-S-In bond at the interface between PdS and In_2S_3 is much more negative (-4.9 eV for on octahedral site and -4.5 eV for tetrahedral site) than that of the Pd-doped In_2S_3 (1.1 eV). Accordingly, PdS loaded on In_2S_3 with bridged S atoms is more stable, and it should be the most likely structure in MI-Pd composites.

To figure out why the interaction between PdS and In_2S_3 is dominant in the composite, DFT calculations were further utilized to analyze the structure stability of PdS bonded with In_2S_3 or MnS. We find that the formation energy of the PdS-In_2S_3 composite is more negative (-4.9 eV, Fig. 6a and Table S5)

than that of the PdS-MnS (-4.1 eV, Fig. 6b and Table S5); therefore, the anchoring of PdS on In_2S_3 in MnS/In_2S_3 is thermodynamically preferable. In addition, we speculate the closer ionic radius of Pd^{2+} (0.84 Å) [57] and In^{3+} (0.91 Å) [58] in contrast to that of Mn^{2+} (0.46 Å) [59] may also attribute to their interaction.

Moreover, to evaluate whether the interaction between PdS and In_2S_3 is more advantageous for the photocatalytic activity than the PdS and MnS interaction, PdS were separately loaded on MnS and In_2S_3. Thus, the influence of PdS on different substances in H_2S splitting was explored. As shown in Fig. 6(c), without MnS/In_2S_3 heterojunction, the photocatalytic performance of MnS or In_2S_3 has decreased a lot. Importantly, introduction of PdS could promote hydrogen evolution efficiency of the pristine In_2S_3 by approximately 10 times, while it only promotes that of the pristine MnS by approximately 2 times. As a result, preferable interaction between PdS and In_2S_3 could make the positive influence of PdS reach the largest extent in MI-Pd composites.
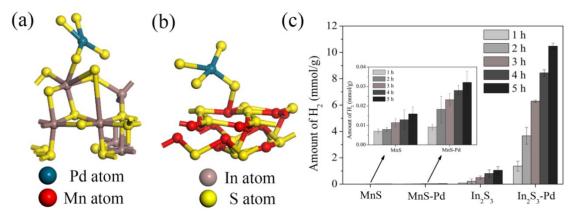

Fig. 6 The model structures of In_2S_3 & PdS interface (a) and MnS & PdS interface (b); photocatalytic hydrogen production over MnS, MnS-Pd, In_2S_3, and In_2S_3-Pd within 5 h. (The added Pd precursor amount is 1.5% which is consistent with MI-Pd 1.5%)(c)

3.3 Significance of PdS in MI-Pd for photocatalysis

In order to investigate the mechanism of promotion of photocatalytic splitting of H_2S by PdS in MI-Pd, a thorough physico-chemical characterization of MI-Pd 1.5% and MI was performed. BET surface area analysis was first carried out to check the possible surface area changes of the two samples (Fig.

S10 and Table S6). It turns out that the surface area of MI-Pd 1.5% (32 m^2 g^{-1}) is a little smaller than that of MI (39 m^2 g^{-1}); therefore, the surface area change with PdS is not the main factor contributing to the improvement activity in MI-Pd. The PL spectra of MI and MI-Pd 1.5% were then recorded. Fig. 7(a) illustrates that PL intensity of MI has obviously decreased in MI-Pd. This reflects the decreased possibility of radiative charge recombination and it is often indicative of promoted charge transfer efficiency of the system in photocatalysis. Such speculation was further supported by SPV measurements (Fig. 7b). Compared with pristine MI, the PdS containing sample displays a much higher photovoltage in the whole measured wavelength range, with a maximum value located at near 390 nm. Additionally, transient photocurrent response of MI-Pd 1.5% is more evident than that of MI (Fig. 7c) and the charge transfer resistance of the MI-Pd 1.5% obtained from the electrochemical impedance spectra (EIS) is smaller than that of the MI (Fig. 7d). Hence, these data altogether provide compelling evidence that PdS in MI-Pd could remarkably improve charge separation efficiency of the MnS/In$_2$S$_3$ composite.
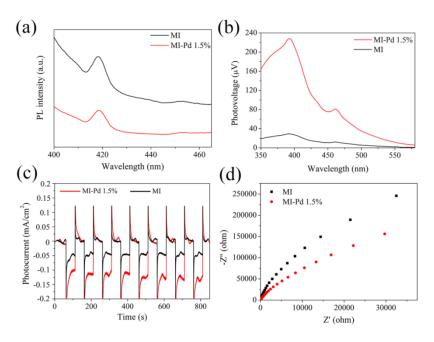

Fig. 7 Photoluminescence spectra (a), surface photovoltage spectra (b), transient photocurrent response test (c), and electrochemical impedance spectra (d) of MI and MI-Pd 1.5%

As surface reaction dynamics is also an important factor influencing the photocatalytic efficiency, the rate of desorption of the initial oxidation product, in particular elemental sulfur, in our system, would also affect the photocatalytic activity of the composite [60]. Accordingly, calculations based on DFT with CASTEP were performed to compare the adsorption energy (AE) of sulfur on PdS with that on the traditional metal co-catalyst Pd (Fig. S11). The results (Table S7) revealed that AE of S on PdS (-3.7 eV) is smaller than that on Pd (-5.5 eV); conversely, desorption of oxidation product sulfur from PdS should be easier than that from Pd. Consequently, introduction of PdS could facilitate the desorption of sulfur to some extent, which ultimately promotes the photocatalytic efficiency of the system as well.

Based on the above analysis, the photocatalytic mechanism could be explained. As shown in Fig. 8, MnS/In_2S_3 is Z-Scheme heterojunction and photogenerated holes are collected on the In_2S_3 side [29]. The photogenerated holes in the composite then transferred to PdS due to the close interaction between PdS and In_2S_3. PdS is widely reported to facilitate hole transfer from metal sulfides to the environment [37], hence, with the preferable anchoring of PdS on In_2S_3, holes could be effectively transferred by PdS during the reaction. Moreover, the special chemical interaction between PdS and In_2S_3 also endow high PdS dispersion on MI, which increases the number of active sites available for catalysis [61-64]. Finally, PdS could also promote the detachment of sulfur from the photocatalyst to some extent.
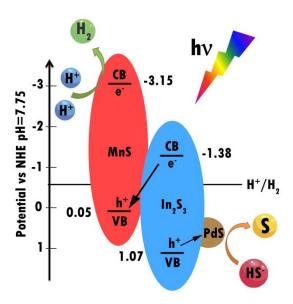
Fig. 8 The band structure and photocatalytic mechanism of MI-Pd under visible light irradiation

3.4 Structure stability of MI-Pd after photocatalysis

As mentioned before, stability is an essential criterion for evaluation of photocatalysts, especially in H_2S rich systems. For this reason, the structure of MI-Pd was characterized after photocatalysis. XRD data manifests that the major diffraction peaks of the original MI-Pd (Fig. S12) remain unchanged. Moreover, TEM results of MI-Pd 1.5% after photocatalysis show that the lamellar structure of MI-Pd is well preserved, and the diffraction rings (Fig. S13b) as well as the exposed lattice planes (Fig. S13c and d) from MnS and In_2S_3 are still discernable. Therefore, the basic structure of MI was maintained during the reaction. Notably, in the XRD pattern, other than original diffraction peaks from MI-Pd, weak peaks related to elemental sulfur emerges. This suggests that sulfur is one of the final oxidation products in our system. Furthermore, XPS shows a very similar result: all the fine spectra of Mn, In and Pd in the MI-Pd 1.5% after photocatalysis remain (Fig. S14) the same, while that of S 2p displays a new signal assigned to S^0. A decline in signal-noise ratio for the fine spectra of Pd 3d can be observed after light irradiation of 5 h, indicating the partial detachment of of PdS in MI-PdS. In combination with the fact that the performance of MI-Pd 1.5% in cyclic experiment is not obviously

influenced after illumination of 15 h, it is conjectured that a part of PdS tightly interacted with In_2S_3 is more crucial for the promotion of efficiency and there is still space for the full utilization of Pd atoms in our system, which is under study now. As for Pd species in the composite after irradiation, the shape of XANES and k^2-weighted EXAFS spectra of Pd from MI-Pd 1.5% before and after photocatalysis (Fig. S15) are identical, suggesting the same coordination environment of Pd in our sample, but still we can see the decreased signal-noise ratio from the sample after photocatalysis, which urges us to further optimize the utilization rate of Pd atom during photocatalysis in the future.

4. Conclusion

In summary, for green conversion of highly toxic H_2S into H_2, MnS/In_2S_3 composite loaded with ultrasmall and highly dispersed PdS was proven to be an effective photocatalyst capable of generating hydrogen. Introduction of PdS in the MnS/In_2S_3 composite significantly increases the hydrogen production rate of the system to 22.7 mmol g^{-1} h^{-1}, with a maximum AQE of 34% at around 395 nm. PdS is well dispersed as XRD and TEM do not present any crystalline PdS in MI-Pd, and detailed analysis of STEM and XPS together with XAS show the existence of well-dispersed PdS. Additionally, the latter analysis indicate the special interaction between PdS and In_2S_3 probably through Pd-S-In bonds at the interface of PdS and In_2S_3. These phenomena are well in line with the recent single-atom related works which revealed chemical interaction of noble metal and substrate [46, 65]. Moreover, the preferable decoration of PdS on In_2S_3 in MnS/In_2S_3 could lead to the remarkably increased activity. Charge separation efficiency and surface reaction kinetics was promoted in the presence of PdS. This work has shown innovative introduction of ultrasmall and highly dispersed PdS on In_2S_3 of MnS/In_2S_3 for photocatalytic splitting of H_2S, and moreover it has demonstrated the importance of the preferable anchoring of PdS on the binary MnS/In_2S_3 composite for efficiency enhancement, which could be further extended to a series of other photocatalysts in the future.

Acknowledgements

Appendix A. Supplementary data

Supplementary data associated with this article can be found in the online version.

Conflicts of interest

There are no conflicts to declare.

References

[1] R.O. Beauchamp, J.S. Bus, J.A. Popp, C.J. Boreiko, D.A. Andjelkovich, P. Leber, CRC Crit. Rev. Toxicol. 13 (1984) 25-97.

[2] N.P. Dasgupta, J.F. Mack, M.C. Langston, A. Bousetta, F.B. Prinz, Rev. Sci. Instrum. 81 (2010) 044102.

[3] I.A. Gargurevich, Ind. Eng. Chem. Res. 44 (2005) 7706-7729.

[4] M. Lashgari, M. Ghanimati, Chem. Eng. J. 358 (2019) 153-159.

[5] A. PiÉPlu, O. Saur, J.-C. Lavalley, O. Legendre, C. NÉDez, Catal. Rev. 40 (1998) 409-450.

[6] X. Zong, J. Han, B. Seger, H. Chen, G. Lu, C. Li, L. Wang, Angewandte Chemie International Edition 53 (2014) 4399-4403.

[7] W. Ma, J. Han, W. Yu, D. Yang, H. Wang, X. Zong, C. Li, ACS Catal. 6 (2016) 6198-6206.

[8] K. Polychronopoulou, F. Cabello Galisteo, M. López Granados, J.L.G. Fierro, T. Bakas, A.M. Efstathiou, J. Catal. 236 (2005) 205-220.

[9] C.A. Linkous, C. Huang, J.R. Fowler, J. Photochem. Photobiol., A 168 (2004) 153-160.

[10] L. Zhang, P. De Schryver, B. De Gusseme, W. De Muynck, N. Boon, W. Verstraete, Water Res. 42 (2008) 1-12.

[11] T. Luo, J. Bai, J. Li, Q. Zeng, Y. Ji, L. Qiao, X. Li, B. Zhou, Environ. Sci. Technol. 51 (2017) 12965-12971.

[12] M. Lashgari, M. Ghanimati, J. Hazard. Mater. 345 (2018) 10-17.

[13] G. Ma, H. Yan, J. Shi, X. Zong, Z. Lei, C. Li, J. Catal. 260 (2008) 134-140.

[14] A. Prakash, M. Dan, S. Yu, S. Wei, Y. Li, F. Wang, Y. Zhou, Sol. Energy Mater. Sol. Cells 180 (2018) 205-212.

[15] J. Zhu, S. Wang, Z. Bian, S. Xie, C. Cai, J. Wang, H. Yang, H. Li, CrystEngComm 12 (2010) 2219-2224.

[16] W. He, Y. Sun, G. Jiang, Y. Li, X. Zhang, Y. Zhang, Y. Zhou, F. Dong, Appl. Catal. B 239 (2018) 619-627.

[17] W. Cui, J. Li, Y. Sun, H. Wang, G. Jiang, S.C. Lee, F. Dong, Appl. Catal. B 237 (2018) 938-946.

[18] W. Cui, J. Li, F. Dong, Y. Sun, G. Jiang, W. Cen, S.C. Lee, Z. Wu, Environ. Sci. Technol. 51 (2017) 10682-10690.

[19] H. Yoshida, L. Zhang, M. Sato, T. Morikawa, T. Kajino, T. Sekito, S. Matsumoto, H. Hirata, Catal. Today 251 (2015) 132-139.

[20] M. Yamamoto, T. Yoshida, N. Yamamoto, T. Nomoto, Y. Yamamoto, S. Yagi, H. Yoshida, J. Mater. Chem. A 3 (2015) 16810-16816.

[21] U.V. Kawade, R.P. Panmand, Y.A. Sethi, M.V. Kulkarni, S.K. Apte, S.D. Naik, B.B. Kale, RSC Adv. 4 (2014) 49295-49302.

[22] Y. Fang, Z. Li, Y. Jiang, X. Wang, H.-Y. Chen, N. Tao, W. Wang, Proc. Natl. Acad. Sci. U. S. A. 114 (2017) 10566-10571.

[23] M. Dan, A. Prakash, Q. Cai, J. Xiang, Y. Ye, Y. Li, S. Yu, Y. Lin, Y. Zhou, Sol. RRL 3 (2019) 1800237.

[24] X.-B. Fan, S. Yu, H.-L. Wu, Z.-J. Li, Y.-J. Gao, X.-B. Li, L.-P. Zhang, C.-H. Tung, L.-Z. Wu, J. Mater. Chem. A 6 (2018) 16328-16332.

[25] L. Cheng, Q. Xiang, Y. Liao, H. Zhang, Energy Environ. Sci. 11 (2018) 1362-1391.

[26] S. Yu, X.-B. Fan, X. Wang, J. Li, Q. Zhang, A. Xia, S. Wei, L.-Z. Wu, Y. Zhou, G.R. Patzke, Nat. Commun. 9 (2018) 4009.

[27] X.-B. Fan, S. Yu, F. Zhan, Z.-J. Li, Y.-J. Gao, X.-B. Li, L.-P. Zhang, Y. Tao, C.-H. Tung, L.-Z. Wu, ChemSusChem 10 (2017) 4833-4838.

[28] M. Dan, Q. Zhang, Y. Zhong, Y. Zhou, J. Inorg. Mater. 32 (2017) 1308-1314.

[29] M. Dan, Q. Zhang, S. Yu, A. Prakash, Y. Lin, Y. Zhou, Appl. Catal. B 217 (2017) 530-539.

[30] Z.H.N. Al-Azri, W.-T. Chen, A. Chan, V. Jovic, T. Ina, H. Idriss, G.I.N. Waterhouse, J. Catal. 329 (2015) 355-367.

[31] B. Li, L. Shao, R. Wang, X. Dong, F. Zhao, P. Gao, Z. Li, J. Mater. Chem. A 6 (2018) 6344-6355.

[32] X. Pan, Y.-J. Xu, J. Phys. Chem. C 117 (2013) 17996-18005.

[33] A.B. Ijzermans, Recl. Trav. Chim. Pays-Bas 88 (1969) 334-343.

[34] A.B. Ijzermans, Recl. Trav. Chim. Pays-Bas 88 (1969) 344-352.

[35] T. Kako, H. Irie, K. Hashimoto, J. Photochem. Photobiol., A 171 (2005) 131-135.

[36] M. Barawi, I.J. Ferrer, J.R. Ares, C. Sánchez, ACS Appl. Mater. Interfaces 6 (2014) 20544-20549.

[37] H. Yan, J. Yang, G. Ma, G. Wu, X. Zong, Z. Lei, J. Shi, C. Li, Journal of Catalysis 266 (2009) 165-168.

[38] J. Yang, H. Yan, X. Wang, F. Wen, Z. Wang, D. Fan, J. Shi, C. Li, J. Catal. 290 (2012) 151-157.

[39] J. Song, H. Zhao, R. Sun, X. Li, D. Sun, Energy Environ. Sci. 10 (2017) 225-235.

[40] C. Ye, M.D. Regulacio , S.H. Lim, S. Li, Q.-H. Xu, M.-Y. Han, Chem. - Eur. J. 21 (2015) 9514-9519.

[41] A. Uzun, B.C. Gates, J. Am. Chem. Soc. 131 (2009) 15887-15894.

[42] J.O. Ehresmann, P.W. Kletnieks, A. Liang, V.A. Bhirud, O.P. Bagatchenko, E.J. Lee, M. Klaric, B.C. Gates, J.F. Haw, Angew. Chem. Int. Ed. 45 (2006) 574-576.

[43] A. Wang, J. Li, T. Zhang, Nat. Rev. Chem. 2 (2018) 65-81.

[44] B. Qiao, A. Wang, X. Yang, L.F. Allard, Z. Jiang, Y. Cui, J. Liu, J. Li, T. Zhang, Nat. Chem. 3 (2011) 634-641.

[45] H. Zhang, G. Liu, L. Shi, J. Ye, Adv. Energy Mater. 8 (2017) 1701343.

[46] P. Liu, Y. Zhao, R. Qin, S. Mo, G. Chen, L. Gu, D.M. Chevrier, P. Zhang, Q. Guo, D. Zang, B. Wu, G. Fu, N. Zheng, Science 352 (2016) 797-801.

[47] A. Zimina, K. Dardenne, M.A. Denecke, D.E. Doronkin, E. Huttel, H. Lichtenberg, S. Mangold, T. Pruessmann, J. Rothe, T. Spangenberg, R. Steininger, T. Vitova, H. Geckeis, J.D. Grunwaldt, Rev. Sci. Instrum. 88 (2017) 113113-113129.

[48] B. Ravel, M. Newville, J. Synchrotron Radiat. 12 (2005) 537-541.

[49] J.J. Rehr, J.J. Kas, F.D. Vila, M.P. Prange, K. Jorissen, Phys. Chem. Chem. Phys. 12 (2010) 5503-5513.

[50] S. Wei, F. Wang, M. Dan, K. Zeng, Y. Zhou, Appl. Surf. Sci. 422 (2017) 990-996.

[51] S. Sinthika, E.M. Kumar, R. Thapa, J. Mater. Chem. A 2 (2014) 12812-12820.

[52] P. Li, F. Wang, S. Wei, X. Li, Y. Zhou, Phys. Chem. Chem. Phys. 19 (2017) 4405-4410.

[53] J.S. Jang, H. Gyu Kim, P.H. Borse, J.S. Lee, Int. J. Hydrogen Energy 32 (2007) 4786-4791.

[54] R. Bhatt, S. Bhattacharya, R. Basu, A. Singh, U. Deshpande, C. Surger, S. Basu, D.K. Aswal, S.K. Gupta, Thin Solid Films 539 (2013) 41-46.

[55] L. Ouyang, P.-f. Tian, G.-j. Da, X.-C. Xu, C. Ao, T.-y. Chen, R. Si, J. Xu, Y.-F. Han, J. Catal. 321 (2015) 70-80.

[56] Y. Li, G. Chen, Q. Wang, X. Wang, A. Zhou, Z. Shen, Adv. Funct. Mater. 20 (2010) 3390-3398.

[57] S.-Y. Wang, N. Li, R.-M. Zhou, L.-Y. Jin, G.-S. Hu, J.-Q. Lu, M.-F. Luo, J. Mol. Catal. A: Chem. 374-375 (2013) 53-58.

[58] S.E. Shirsath, B.G. Toksha, K.M. Jadhav, Mater. Chem. Phys. 117 (2009) 163-168.

[59] M. Liu, L. Zhang, X. He, B. Zhang, H. Song, S. Li, W. You, J. Mater. Chem. A 2 (2014).

[60] M. Dan, S. Wei, D.E. Doronkin, Y. Li, Z. Zhao, S. Yu, J.-D. Grunwaldt, Y. Lin, Y. Zhou, Appl. Catal. B 243 (2019) 790-800.

[61] X. Zhang, J. Guo, P. Guan, C. Liu, H. Huang, F. Xue, X. Dong, S.J. Pennycook, M.F. Chisholm, Nat. Commun. 4 (2013) 1924.

[62] P. Yin, T. Yao, Y. Wu, L. Zheng, Y. Lin, W. Liu, H. Ju, J. Zhu, X. Hong, Z. Deng, G. Zhou, S. Wei, Y. Li, Angew. Chem. Int. Ed. 55 (2016) 10800-10805.

[63] H. Yan, H. Cheng, H. Yi, Y. Lin, T. Yao, C. Wang, J. Li, S. Wei, J. Lu, J. Am. Chem. Soc. 137 (2015) 10484-10487.

[64] J. Xing, J.F. Chen, Y.H. Li, W.T. Yuan, Y. Zhou, L.R. Zheng, H.F. Wang, P. Hu, Y. Wang, H.J. Zhao, Y. Wang, H.G. Yang, Chem. - Eur. J. 20 (2014) 2138-2144.

[65] X. Wu, H. Zhang, J. Dong, M. Qiu, J. Kong, Y. Zhang, Y. Li, G. Xu, J. Zhang, J. Ye, Nano Energy 45 (2018) 109-117.